Computational Noise Prediction from Trailing Edge Flows

Zane Nitzkorski and Krishnan Mahesh
(University of Minnesota, USA)

ABSTRACT

We characterize the impact of near-field turbulence and boundary layer thickness for a 45° beveled trailing edge by investigating two different inflow boundary layer thicknesses. Noise from this type of scenario is important for propellers, airfoils, fans and marine propulsors. This geometry has been investigated experimentally by Olson and Mueller (2004) and Shannon and Morris (2006), Shannon et al. (2006) and computationally by Wang (2005) but boundary layer sensitivity has not been studied previously. Large-eddy simulation (LES) is performed at the experimental boundary layer conditions as well as a boundary layer momentum thickness ξ which is eighteen times smaller. A porous Ffowcs-Williams and Hawkings (FWH) Ffowcs-Williams and Hawkings (1969) acoustic analogy is used to solve for the far-field noise and shows good agreement with experimental results. The acoustic analogy is compared to a Curle based formulation where the surface terms are used as the sources in conjunction with a specialized half-plane Green's function. The scaling of noise production with the physical properties which produce acoustic sources are discussed. Comparing and contrasting the two boundary layer thicknesses demonstrates that the noise produced in the lower half plane is fairly insensitive to boundary layer thickness because of the shedding vortex. The noise produced in the upper half plane however is strongly related to the boundary layer thickness. The separation point is similar between both cases, but the near field turbulent intensities contribute to the increased noise for the thicker boundary layer case.

INTRODUCTION

Trailing edges of airfoil sections are ubiquitous in aeronautical and hydrodynamic applications, and understanding the noise generation process for this configuration is therefore important. The production of sound depends on the geometry of the body as well as the boundary layer. These two factors interact as the body modifies the near field turbulence and provides the mechanism to scatter the flow energy and radiate it efficiently as acoustic energy. In order to characterize the noise production dependence on the boundary layer, LES computations are performed for a trailing edge geometry with two different boundary layer thicknesses. The flowfield and sound field is dominated by the separation of the boundary layer. As the flow accelerates over the top of the body it sets up a periodic shedding characterized by a fluctuating pressure and velocity near the airfoil which subsequently radiates to the sound field. The fluctuations near the trailing edge tip are related to the boundary layer thickness and account for the sound intensity.

Motivation for the current investigation comes from two similar trailing edge configurations which have been studied experimentally and computationally. The first configuration was largely studied by Blake (1975) where trailing edges of 25° and 45° were studied. The 25° case produced tonal non-fixed coherent shedding and lacked acoustic comparison data, so the second beveled trailing edge at 45° was studied in more depth by Blake (1986), Gershfeld et al. (1988), and summarized in Blake and Gershfeld (1989). Additional experiments were conducted more recently to examine the sound field by Olson and Mueller (2004), Shannon and Morris (2006), and Shannon et al. (2006). These found a strong phase behavior to the shedding that directly relates to the recovered sound.

The shedding behavior described in Blake (1975) provides a detailed look at the separation mechanism, pressure correlation, and velocities in the separated wakes. The frequency content associated with the flow near the trailing edge as well as the root mean square of the pressure at the surface provide the scaling associated with received sound to these quantities. Blake and Gershfeld (1989) use these correlations combined with traditional dipole scattering relations to predict acoustic pressure and the ratio of scattered noise to that if directly radiated.

We use these relations to investigate the effect of the change in boundary layer thickness.

Computational studies have been performed to investigate the noise from trailing edges. These include Wang and Moin (2000) who studied the 25° trailing edge corresponding to the work of Blake (1975) and found comparable trends to the work of Gershfeld et al. (1988). Manoha et al. (2000) investigated noise from a flat plane and demonstrated the need for a specific Green's function if surface terms are used for a Curle type acoustic analogy. Oberai et al. (2002) studied scattered noise from airfoils by comparing the scattered noise from prescribed quadrupoles near the trailing edge to a LES performed for the airfoil geometry. A much thinner trailing edge that was excited by a vortex generator slightly upstream was computed using a porous FWH method by Singer et al. (1999). Marsden et al. (2007) investigated the optimal shape change for the 45° configuration to reduce the shed vorticity and as a result the noise.

PROBLEM DESCRIPTION

We simulate, using LES, the experiment by Olson and Mueller (2004) where a 45° beveled airfoil of height h and chord $c = 18h$ is placed halfway into the exit nozzle of a low speed $M = 0.1$ flow at a Reynolds number $Re_c = \frac{\rho U c}{\mu} = 1.9\text{x}10^6$, $Re_h = \frac{\rho U h}{\mu} = 105,555$ based on height, such that $9h$ is outside of the nozzle. Half of the airfoil is simulated as well as an extended wake region. In the experiment a microphone array is positioned at a distance of $20h$ away and is arranged to capture a corrected noise component roughly perpendicular to the trailing edge point. The LES simulation solves the incompressible LES equations by applying the filter operation to the Navier-Stokes (N–S) equations and with the closure terms modeled using the surrogate correlation time scale Lagrangian averaging scheme for the dynamic Smagorinsky model developed by Verma and Mahesh (2012). An example flow visualization is shown in figure 1 which shows the turbulent wake.

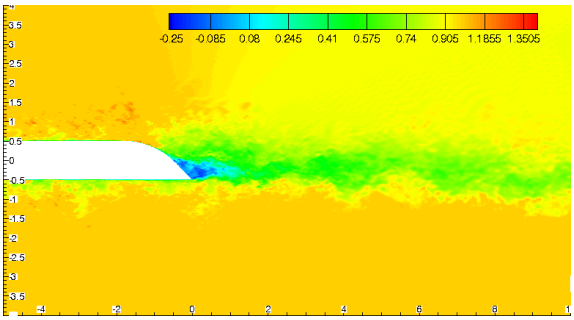

Figure 1: Trailing edge problem visualization using the instantaneous u-velocity.

Computational Solution Methodology

The governing equations for a fluid are the Navier–Stokes (N–S) equations:

$$\begin{aligned} \frac{\partial u_i}{\partial x_i} &= 0, \\ \frac{\partial u_i}{\partial t} + \frac{\partial u_i u_j}{\partial x_j} &= -\frac{\partial p/\rho}{\partial x_i} + \frac{\partial \tau_{ij}}{\partial x_j}, \end{aligned} \tag{1}$$

where the density has been absorbed into the pressure term.

In LES, the large energy carrying scales of turbulence are directly resolved on the computational grid and the effect of the smaller scales is modeled. The flow variables are decomposed into large scales (denoted by $\overline{(\cdot)}$) and small scales (denoted by $(\cdot)'$). Applying the filter operation to the N–S equations and assuming commutation with the spatial derivatives yields the filtered N–S equations:

$$\begin{aligned} \frac{\partial \overline{u}_i}{\partial x_i} &= 0, \\ \frac{\partial \overline{u}_i}{\partial t} + \frac{\partial}{x_j}(\overline{u}_i \overline{u}_j) &= -\frac{\partial \overline{p}}{\partial x_i} + \nu \frac{\partial^2 \overline{u}_i}{\partial x_j \partial x_j} - \frac{\partial \tau_{ij}}{\partial x_j}, \end{aligned} \tag{2}$$

where $\overline{(\cdot)}$ denotes the filtered flow variable at scale Δ and $\tau_{ij} = \overline{u_i u_j} - \overline{u}_i \overline{u}_j$ is the sub–filter scale (SFS) stress which in our implementation uses grid–filtered LES, meaning $SFS = SGS$. The SGS stress τ_{ij} which are needed close eq. 2 are modeled using the surrogate correlation time scale Lagrangian averaging scheme for the dynamic Smagorinsky model developed by Verma and Mahesh (2012).

Acoustic Analogy Methodology

A porous FWH acoustic analogy Ffowcs-Williams and Hawkings (1969) is used to obtain the far-field noise at $\mathbf{x}$ from the near field, $\mathbf{y}$. The porous FWH

analogy works by aggregating sources derived from flow quantities on a tagged data surface with outward pointing normal $\mathbf{n}$ and uses a Green's function to propagate that effect to the far-field. The Navier-Stokes (N–S) equations are rearranged into an inhomogeneous wave equation for the fluctuating pressure as

$$\begin{aligned} p'(\mathbf{x},t) = & \frac{1}{4\pi|\mathbf{x}|}\frac{\partial}{\partial t}\int Q_i\left(\mathbf{y},t_{ret}\right)n_i dS \\ & - \frac{x_i}{4\pi c_0|\mathbf{x}|^2}\frac{\partial}{\partial t}\int L_{ij}\left(\mathbf{y},t_{ret}\right)n_j dS \\ & + \frac{x_i x_j}{4\pi c_0^2|\mathbf{x}|^3}\frac{\partial^2}{\partial t^2}\int_{V_{ext}} T_{ij}\left(\mathbf{y},t_{ret}\right)dV. \end{aligned} \tag{3}$$

where the emission time is $t_{ret} = t - \frac{|\mathbf{x}|}{c_0} + \frac{\mathbf{x}\cdot\mathbf{y}}{c_0|\mathbf{x}|}$

The thickness, loading, and volume terms are expressed as

$$Q_j = \rho_0 v_j + \rho(u_j - v_j), \tag{4}$$

$$L_{ij} = \rho u_i(u_j - v_j) + \Delta P_{ij}, \tag{5}$$

$$T_{ij} = \rho u_i u_j + P_{ij} - c_0^2(\rho - \rho_0)\delta_{ij}, \tag{6}$$

where T_{ij} is the Lighthill stress tensor, e.g. Lighthill (1952), $u_n = u_i n_i$ and $v_n = v_i n_i$ are the velocity of the fluid and the surface respectively, and $P_{ij} = (p - p_0)\delta_{ij} - \tau_{ij}$ is the compressive and viscous stress tensor. The terms are computed either at the FWH surface or in the exterior volume.

The implementation of equation 3 depends on specifying integration surfaces and volumes. The FWH surfaces are prescribed on background unstructured grids, which makes arbitrary surface extraction within the computational domain challenging. We define arbitrary surfaces and discretize the surface in a manner that reflects the volume grid in the interior. We accomplish this by projecting the centroids of the volume grid on the FWH surface and then generate a constrained Delaunay triangulation for the connectivity while its mesh dual, the Voronoi diagram, provides the projected face areas. Finally, we establish exterior and interior volumes which allow for surface integration to be handled in tandem with consistent volume integration.

In addition, a dynamic endcap procedure is utilized to get the flux corrected surface terms as described in Nitzkorski and Mahesh (2014). Here these projected partner pairs are correlated to establish a convection velocity which can be a function of the spatial extent. This approach takes the concepts suggested by Wang et al. (1996) in terms of volume fluxes and applies them to surfaces terms by assuming that the primary cause of the error is a truncation error due to a finite domain which can be corrected on the porous FWH surface. Truncation errors and the corrections within this framework were also investigated by Sinayoko et al. (2015). The flux correction function is constructed as,

$$\begin{aligned} \ddot{T}_{ij}(t) = & \frac{\partial^2}{\partial t^2}\int_{V_0} T_{ij}(y,t_{ret})\mathrm{dy}^3 \\ & + \frac{\partial}{\partial t}\int_{S_{ext}} U_c T_{ij}(y,t_{ret})\mathrm{dy}^2. \end{aligned} \tag{7}$$

The corrective flux $\frac{\partial}{\partial t}\int_{S_{ext}} U_c T_{ij}(y,t_{ret})\mathrm{dy}^2$ is applied at the exit surface of the bounding volume in order to approximate the missing sources exterior to the surface of integration.

We dynamically calculate the model constant, U_c, by correlating the the correction term over subsequent exit planes with the projected pair partners with the element normal $\hat{n}_k$. The distance between the elements $dx_{j,k}$ establishes a correlation function based on the corrective flux to compute U_c as

$$U_c = \sum_{j=0,k=0}^{N_j,N_k} \frac{dx_{j,k}\cdot\hat{n}_k}{max(\frac{\beta(t)\hat{R}_{xy}(m)}{N})dt}, \tag{8}$$

with correlation function

$$\hat{R}_{xy}(m) = \begin{cases} \sum_{n=0}^{N-m-1} \alpha x_{n+m}\, y_n^* & m \geq 0 \\ \hat{R}_{xy}^*(-m) & m < 0 \end{cases}. \tag{9}$$

The multiplying factor $\beta(t)$ is a windowing function in time which ensures only one maximum correlation over any given averaging period and an optional multiplying term α allows to normalize the signal's strength before the correlation to account for decay in the signal over longer separation distances. Obtaining the convection velocity via correlation as opposed to from the time–averaged flow–field ensures its application to non–stationary problems and situations such as gusting inflow and curved bounding surfaces.

Acoustic Analogy Validation

In order to validate the FWH acoustic analogy we computed noise from a $Re = 89000$ cylinder and compared the results to experimental data of Revell et al. (1977) who placed a cylinder into the exhaust of a nozzle and captured the noise with a microphone array and the unsteady Reynolds–averaged Navier–Stokes(URANS) computation of Cox et al. (1998). The noise data was computed using $180D/U_\infty$ units

of time and the Nyquist frequency was 500 Hz. The noise at $\theta = \pi/2$ and $r = 128D$ as shown in figure 2 shows good agreement at the fundamental frequency as well as the drag and first lift harmonic. The first lift harmonic for the current results show some shift relative to the experiment but our results show the frequency at $f \approx 3f_0$ where the first overtone of lift should reside. In contrast, the URANS predicts no harmonics of lift and drag since it is a 2D computation and has a larger shift in the Strouhal frequency, $St = f_0 U/h$, relative to current results. The sound field is visualized by solving the FWH equations at a fixed time throughout the domain and the wake is visualized by λ_2 in figure 3. It is clear that the principal source of sound is associated with the cylinder body and that the wake provides higher frequency content. Overall the agreement with experiment is quite good and significantly better than the URANS.

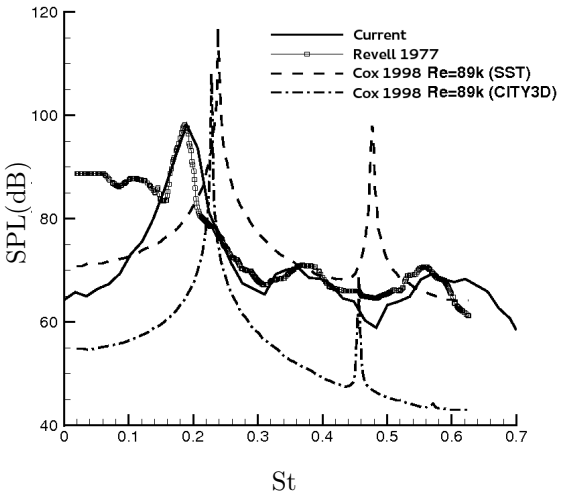

Figure 2: The frequency content of the generated noise, SPL(dB) vs frequency, at the location $\theta = \pi/2$ and L=128D is compared to the experiments of Revell et al. (1977) and the computations of Cox et al. (1998).

Computational Setup

The simulation domain was $x/h = [-9, 35]$, $y/h = \pm 20$, and $z/h = 20$ with 150 points discretizing the span and approximately 72 million total control volumes. The wall spacing was $\Delta n = 2.5\text{x}10^{-5}$ near the trailing edge and $\Delta n = 5\text{x}10^{-4}$ in the boundary layer. A timestep of $\Delta t = 5\text{x}10^{-5}$ was used. The trailing edge tip was rounded with a radius of $0.0005h$ and an extra dense region within a normal distance of $2h$ from the wall was used to resolve the

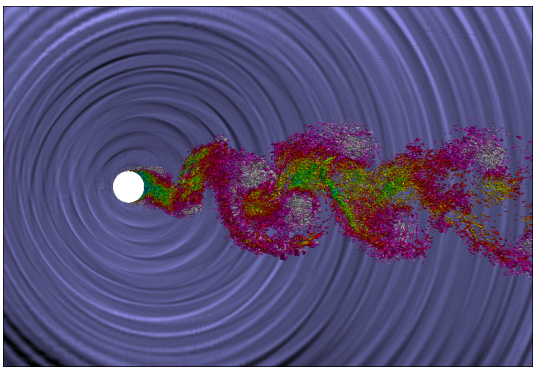

Figure 3: An iso-surface of λ_2 colored by u-velocity and the sound field is visualized by solving the FWH equations for a $Re = 89,000$ cylinder.

separation and wake interaction. The acoustic calculations have been performed with a porous FWH implementation with the porous surfaces located $1.5h$ away from upper and lower surfaces and $1.5h$ downstream of the trailing edge point. The grid refinement in this area provides high quality resolution resulting in almost a third of all processors having control volumes cut by these porous surfaces. A second series of FWH surfaces were placed $5h$ downstream to ensure convergence and the computed noise varied negligibly so the nearer FWH surfaces are used for reported data. A grid schematic is shown in figure 4 which also shows the FWH planes.

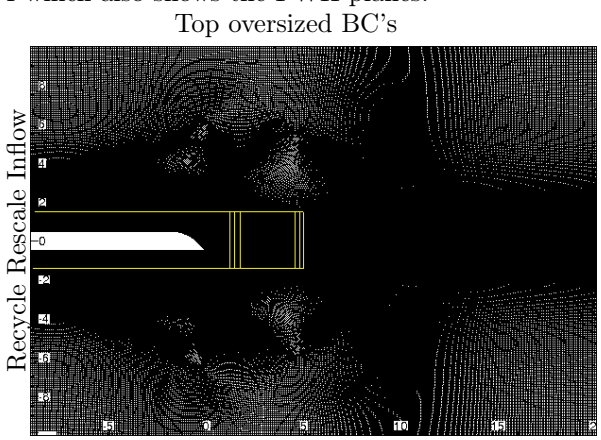

Figure 4: A schematic of the grid with FWH planes shown in yellow.

Freestream boundary conditions when applied to the top and bottom were found to not produce the correct mean pressure distribution along the airfoil for this computational domain. Therefore an oversized domain, including the upstream section,

of $(x/h, y/h) = \pm 100$ was used and a semi-cylinder fore-body for the airfoil was simulated. Since the entire airfoil was simulated and the domain was significantly larger than the body a far-field condition of $u = u_\infty$ was applied on the inflow as well as the top and bottom. An outflow Neumann condition was applied at the exit and periodicity enforced in the span. The pressure distribution along the airfoil significantly improved with this simulation, so the time averaged mean velocity at the location of the top and bottom of the smaller domain was extracted and applied as the far-field boundary condition for the finer calculation. The u-velocity on the upper boundary was represented by a fifth order polynomial whereas v-velocity on the top and u, v-velocities on the bottom were solved with a ninth order polynomial. This procedure is similar to that of Wang (2005) and Marsden et al. (2007) who used a RANS simulation performed on a much larger domain and also found the pressure distribution to be in closer agreement. The effect of this approach on C_p along the airfoil is shown in figure 5.

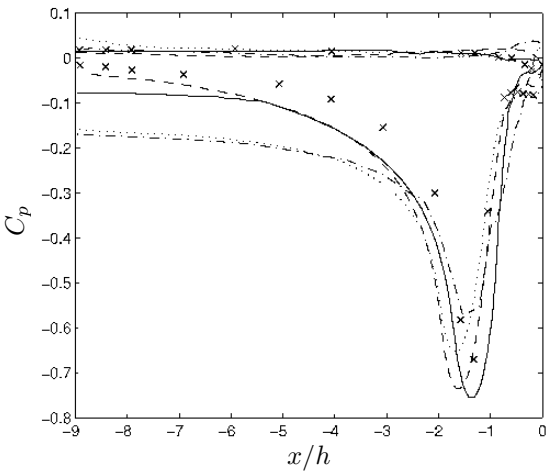

Figure 5: Coefficient of pressure from all the methods: (–) current with adjusted BCs, (-.) current with freestream BCs, (x) Olson and Mueller (2004), (− −) Wang (2005) with adjusted BCs, (. . .) Wang (2005) freestream BC.

The recycle-rescale methodology of Lund et al. (1998) with momentum height ξ was employed on both the upper and lower surfaces of the trailing edge with a prescribed $Re_\xi = \frac{\rho U \xi}{\mu} = 1895$ and 1760 respectively, consistent with Wang (2005) for the experimental thickness case. For the thinner case the inflow Re_ξ was eighteen times smaller. The recycle plane was set to be $x/h = 1.75$ or approximately $10\delta_{upper}$ downstream of the inflow condition. The vertical extent of the recycle domain is 1.5δ, which is smaller than the vertical extent of the computational domain. Therefore, at the inflow plane, the recycle values are prescribed at y-locations smaller than the vertical extent of the recycle domain. At larger y locations, the streamwise velocity is set to its freestream value and the vertical velocity is obtained from a quadratic curve constrained by the vertical velocities at the top of the recycle domain and the computational domain respectively.

The noise was calculated at $(x/h, y/h) = (3, 21)$ above the trailing edge for point SPL comparisons with the experiment and at a 180 points with a radius of $100h$ for directivity with total sampling time from start to finish of $\Delta T = 100$ and a sampling timestep of $\Delta t = 5e-5$ giving a spectral discrimination of 0.01Hz and a Nyquist frequency of $10,000$Hz. In the experiment a 10Hz pass band filter with a Nyquist frequency of 4000Hz was used as opposed to our approach with a Hann filter using 50% overlapping. Wake data as well as available noise data is compared to Wang (2005) and Olson and Mueller (2004). Additional noise calculations such as sound sources both on the trailing edge as well as within the wake are presented.

RESULTS

For each of the boundary layer thicknesses the flow field is analyzed and in the case of the experimental thickness, compared to computational and experimental data. After this, the acoustics for the experimental thickness are discussed and compared with available data. Then the smaller boundary layer acoustic data is compared and contrasted with the thicker boundary layer. The combined results are analyzed together to establish the change in noise production and the reason for this difference.

Flow-field validation

The experimental boundary layer thicknesses on the top and bottom are $\delta_{99} \approx 0.1712h$ and $0.1642h$ respectively. The boundary layer profile comparisons along the upper surface boundary are shown in figure 6. A set of follow-on experiments to the work by Olson and Mueller (2004) was conducted by Shannon and Morris (2006). They found that dominant phase behavior indicating a dominant frequency was present. The St number for the principal oscillation of the wake was found by Shannon and Morris (2006) to be 0.42, Olson and Mueller (2004) found

0.40, Wang (2005) to be 0.44, and we calculate it at 0.41.

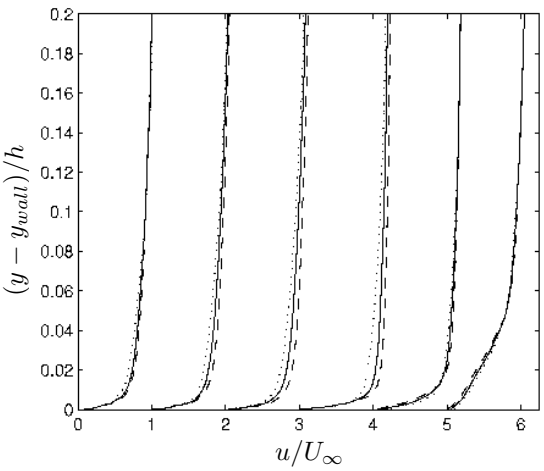

Figure 6: Comparison of the boundary layer at x-locations of $x/h = -7.5, -3.5, -2.5, -1.625, -1.25$, and -0.875 shown with an offset, between (–) current, (- -) Wang (2005), $(\cdots)$ Olson and Mueller (2004).

The mean streamwise wake profiles downstream of the trailing edge are shown in figure 7 which show close agreement between all methods. The evolution of the rms values of u-velocity are shown in figure 8. It is clear that the wake and the fluctuations near the wake edge are accurately captured. This would suggest that the flowfield fluctuations in the experiment and those in the simulation are directly related and since these fluctuations and pressure fields determine the noise that sound should be comparable.

There are no direct comparisons which can be made to validate the flow-field for the thinner boundary layer. A flow visualization showing the u-velocity which clearly demonstrates the thinness of the boundary layer is shown in figure 9. This is further reinforced with the boundary layer profile comparison in figure 10 which shows how much thinner. The momentum thickness θ is initialized to be 18 times thinner but grows faster to be only 12 times thinner at $x/h = 3$ before the acceleration over the trailing edge thins the boundary layer again. Also note how the boundary layer at $x/h = -1.625$ close to the beginning of the bevel thins much faster than in the thicker case.

Acoustic sources

The acoustic sources can be decomposed for further investigation to their principal components of

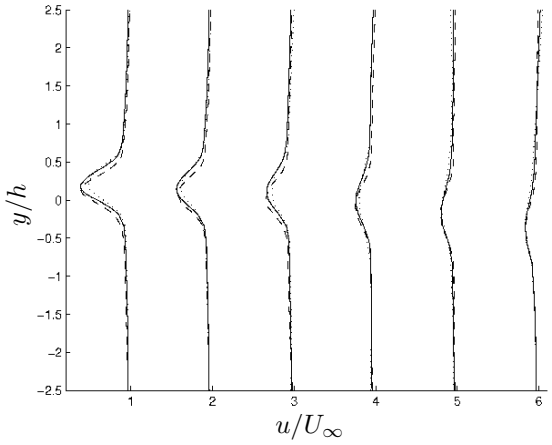

Figure 7: Mean u-velocity wake profiles between (–) current, (- -) Wang (2005), $(\cdots)$ Olson and Mueller (2004), shown with an offset at wake x-locations $x/h = 1, 1.5, 2, 3, 4, 6$

the fluctuating surface pressure and the Lighthill stress tensor in the volume. The source terms in the volume stress tensor are principally the Reynolds stresses which are related to the Lamb vector, the cross product of vorticity and velocity, $\vec{\omega} \times \vec{u}$. The acoustic sources for both are examined using the time average of their absolute values.

The surface terms are described by the loading term and are most strongly influenced by the pressure fluctuations dp/dt. In figure 11 the surface forces are approximated by the mean of $|dp/dt|$ at every location dot multiplied with the local normal to give magnitude of the fluctuating pressure. It is clear that the trailing edge point produces most of the pressure fluctuations and therefore is the strongest source of sound, however, for the thicker boundary layer a significant amount of fluctuating pressure occurs near the separation point. Related, the thinner boundary layer with the later separation shows much less source contributing over the top of the bevel.

The volume sources are directly related to the Reynolds stresses. The region of activity for both components in both extent and magnitude have diminished for the smaller boundary layer case. Note that the truncation which appears in the near-field is due to the extraordinarily fine region of resolution which wraps body at a distance of $2h$ away from the surface.

The time averaged volumetric source fields are shown in figures 13 and 14 and show similarities to the Reynolds stress fields. These regions are associated with the Reynolds stress component $\overline{u'u'}$ in par-

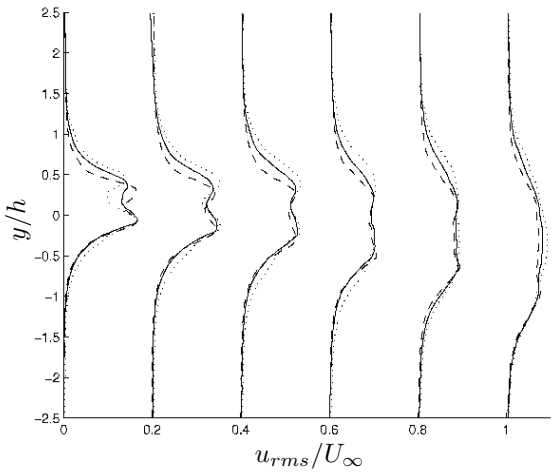

Figure 8: Mean u-velocity rms wake profiles between (–) current, (- -) Wang (2005), ($\cdots$) Olson and Mueller (2004), shown with a 0.2 offset at wake x-locations $x/h = 1, 1.5, 2, 3, 4, 6$

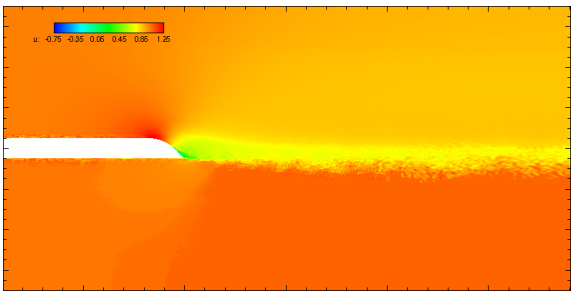

Figure 9: A visualization of the thin boundary layer case of u-velocity.

ticular, as the vorticity is released from the wall and is accelerated in the downstream direction. Therefore the large magnitude vorticity vectors are nearly perpendicular to the background velocity which produce large amounts of noise. The sources of sound for the thin boundary layer case are similar to those of the larger case, except decreased in amplitude and extent. The noise production associated with the shear layer on the upper surface is diminished due to the thinner momentum thickness layer which interacts over a shorter length. The ejection of the the lower boundary layer shows that the magnitude for the thinner case is slightly diminished but is still fairly similar to the thicker boundary layer in this region.

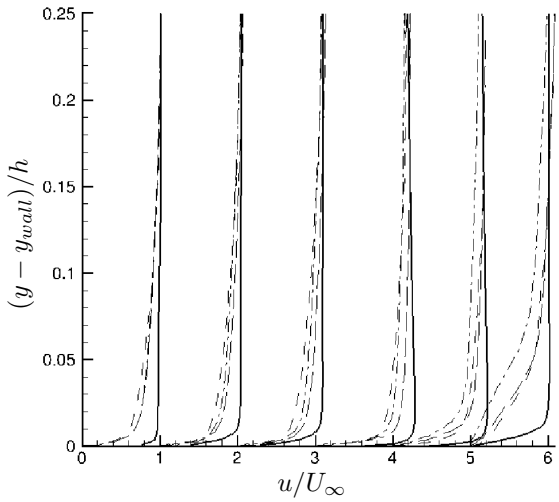

Figure 10: Boundary layer profiles compared with the thicker case.

Acoustic results and effect of boundary layer thickness

The noise production from both boundary layer thickness cases are evaluated by examining the point spectra at a given location. The noise at a point $(x/h, y/h) = (3, 21)$ in the is shown in figure 15. Also shown is the experimental measurement obtained using a two-point acoustic array. The Nyquist frequency of the experiment is 4000 Hz and a 10 Hz passband filter is applied to the data; in contrast, the Nyquist frequency of the computations is 100000 Hz and no passband filter is used. The thick boundary layer case shows good agreement with experiment. The mismatch at low frequencies is characteristic of such comparison across computational data, posited to be ambient low frequencies. At high frequencies the simulations capture more sound due to the higher Nyquist frequency which is also higher than that of Wang (2005).

DISCUSSION

We have established that the fluctuating pressure scattered by the surface and the near field turbulence serve as sources the far-field acoustic pressure. The scaling laws which relate these quantities were thoroughly described by Blake (1975) and Blake and Gershfeld (1989) associated with fluctuating pressure strength and pressure velocity correlations in the turbulent wake and scattered to the far-field as described by Williams and Hall (1970) for the trailing edge case.

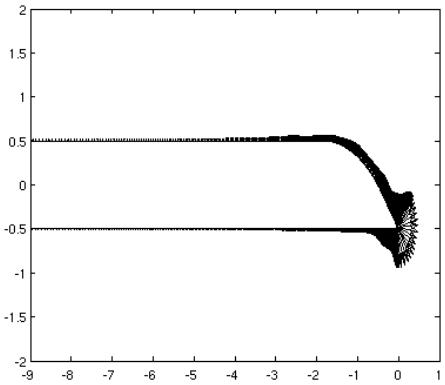

(a)

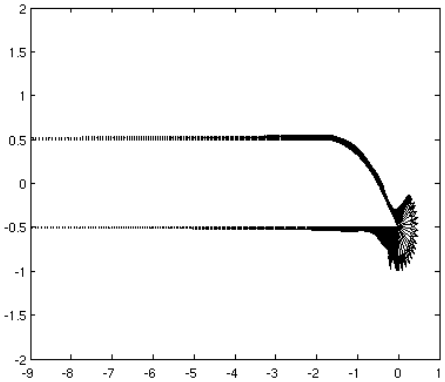

(b)

Figure 11: Major component of the surface sources, $|dp/dt|$, plotted as the magnitude of the vectors for for (a) experimental boundary layer case and (b) thin boundary layer case.

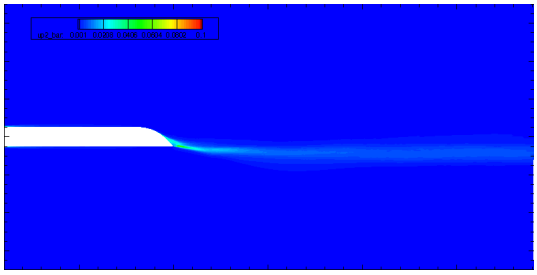

(a)

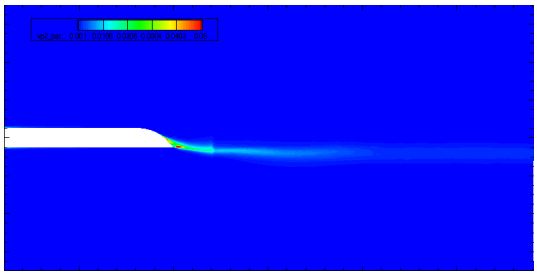

(b)

Figure 12: Reynolds stress components (a) $\overline{u'u'}$ and (b) $\overline{v'v'}$ for the thin boundary layer case are shown.

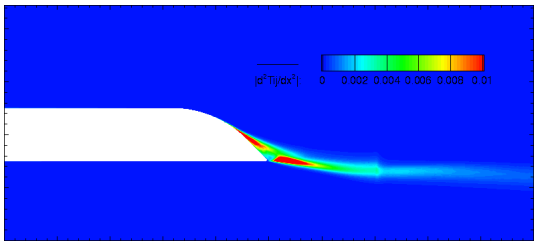

Figure 13: Mean of $|\partial^2 T_{ij}/\partial t^2|$ for thin boundary layer case.

It was shown by Blake (1975) for the 45° case that the pressure frequencies found in the near field contained similar content, but that at non-peak frequencies they quickly diminished even at $x/h = 1.1$ away from the test body. The fluctuating pressure had higher rms values near the body as well as more distinguished overtones. We use this near field fluctuation for investigation by examining the normalized pressure in the near field $(x, y) = (0.5, 0)$, shown in figure 16 and comparing it against the surface forces shown in figures 11 for their location intensities. The Blake experiments had two velocities, $U_\infty = 15.24, 30.48$m/sec, and found that for the lower speed with the thicker boundary layer that average prms was 2.3 times higher due to the increase in the broadband components. The tonal quality at this lower speed however was not as prominent and this provided the explanation that the two principal sources were the periodic ejection of vorticity causing the tonal pressure fluctuations associated with a scattered dipole and the setting up of the convecting Helmholtz vorticity in the near field which radiates in a broadband fashion.

Interestingly, in the experiments, doubling the mean background velocity had an amplifying effect on the fluctuating components, but the overall Strouhal frequency did not shift. This implies that the body shape was highly responsible for the type of shedding for these geometries. Blake and Gershfeld (1989) provide a diagram showing which characteristics govern source production for a range of Reynolds numbers and angles of attack conditioned

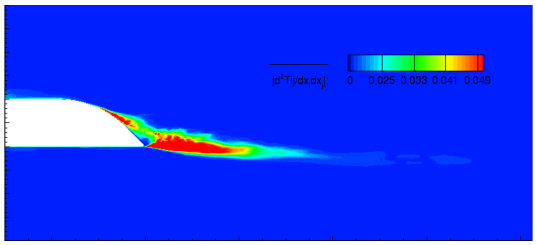

Figure 14: Volumetric sound sources for experimental boundary layer case.

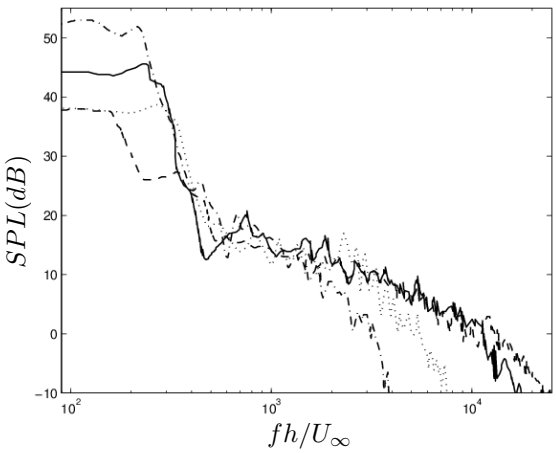

Figure 15: Comparison of noise from (–) current thick, (- -) current thin, (-.) Olson and Mueller (2004), and (· · ·) Wang (2005)

on the body shape.

In the experiments of Blake (1975), the pressure-velocity correlations for the 45° case at $U_\infty = 30.48$m/sec and $Re = 1.9\text{x}^6$ were fairly constant with some subtle curvature variation only in the first $1.5h$. This correlation in the upper shear layer was used to identify the transition region based on the recovery distance. The vortex was found to shed in the first $1.38h$ with a recovery/pairing off zone that lasted till $2.1h$ after which the correlation was monotonic. It is over this length scale in the setup region that our results indicate Lighthill tensor based contributing sources due to the wake velocity being different from the convection velocity, acting on the vorticity released form the body as the the von Karman street is established.

As formulated by Blake and Gershfeld (1989), the relation between the received (r) and surface

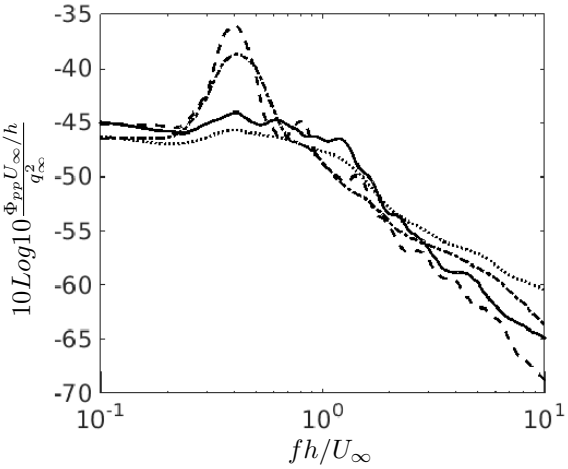

Figure 16: The pressure spectrum variation between a point on surface $x_1/h = (-.375, .375)$ and a point in the near-field $x_2 = (0.5, 0)$ referenced off the trailing edge for both boundary layer thicknesses: (- -) Thick x_1, (-.) Thick x_2, (–) Thin x_1, (...) Thin x_2.

,

source (s) fluctuating pressure is,

$$\frac{\overline{p_r^2}(\vec{r},\omega_s)}{\overline{p_s^2}(y_1)} \approx \frac{1}{2\pi^2}\frac{U_\infty}{c_0}\frac{2L_3}{y_f}\frac{|y_1-y_s|\Lambda_3}{r^2}|\sin\phi|\sin^2\frac{\theta}{2}, \tag{10}$$

where y_f is the approximate thickness of the wake as measured by fluctuating velocity, $y_1 - y_s$ is the distance between the fluctuation on the surface and the separation point, Λ_3 is the spanwise correlation length and the angles θ for the in-plane angle and ϕ for the out of plane angle. We use equation 10 to estimate the impact of the change in boundary layer thickness between the thick and thin cases. The ratio of wake thicknesses is $y_{f,rat} \approx 0.68h/0.11h = 6.2$. By using the normalized fluctuation strength along the surface and averaging at the distances from the trailing edge tip we estimate the ratio of $|y_1 - y_s|_{rat} \approx .63h/.27h = 2.33$. Gershfeld calculates the spanwise correlation distance by using boundary layer edge values, but we lacking that we estimate the correlation from the surface pressures to roughly obtain the ratio of $\Lambda_{3,rat} \approx .8$. Therefore the estimated difference in acoustic pressure is 5.22dB which is comparable to the found 5.45dB difference. This corresponds to the low frequency offset and it should be noted in figure 15 that the noise does not have a distinct peak frequency for the thin boundary layer case and that the decibel level drops quite quickly to much lower level over a broad range of frequencies.

The broadband components are also discussed by Blake and Gershfeld (1989) associated with the analytical expansion by Howe (1975) for the acoustic pressure with regard to maintaining the Kutta condition for a half-plane. The derived governing equation is,

$$p_a(x,t) = \frac{\rho_0 \Gamma_3 U_c \sin(\theta/2)}{2\pi\sqrt{r}} \left(1 - \frac{U_w}{U_c}\right) \left[\frac{\cos\theta_0/2}{r_0^{1/2}}\right]_{t_{ret}}, \tag{11}$$

where Γ_3 is the circulation of the spanwise vortex coming off the trailing edge and U_c and U_w are the convection velocity and the wake velocity respectively. θ is directivity angle in the plane running parallel to the inflow and θ_0 is the polar angle. If the wake and convection velocity are the same, no noise would be produced, but as observed by Yu and Tam (1978) usually $U_w = 0.6U_c$. Also of note is how the broadband components are not influenced by the thickness of the wake, but by the velocity scales. Specifically, since we reduced the physical height of the boundary layer, but not the velocity, the changes in the strength of the vorticity Γ_3 is nearly inversely proportional to the difference in convection and wake velocity $U_c - U_w$ meaning that the broadband components between the two cases vary little. This is different from the experiments of Blake and Gershfeld (1989) where the velocity was varied and results in a non-linear difference between the vortical strength and the wake velocity characteristics. This mechanism explains the close agreement between the broadband components for our two boundary layer cases.

EFFECT OF GREEN'S FUNCTION

A significant motivation to develop the porous FWH methodology is that it enables the use of the free-space Green's function irrespective of geometrical complexity. In this section we demonstrate the reasonableness of this approach by comparing the sound prediction to that obtained using only the surface terms and half-plane Green's function. The half-plane Green's function provides a good representation for the trailing edge. It was described by Williams and Hall (1970); from which Crighton (1972) then provided a two-dimensional compact Green's function representation. Howe (1975) then represented the Green's function in physical space using the method of stationary phase to achieve,

$$\begin{aligned} G(\mathbf{x},\mathbf{y},t-t_{ret}) &\approx \frac{\varphi(\mathbf{x})\varphi(\mathbf{y})}{4\pi|x|}\delta(t-t_{ret}), \\ \mathbf{x} &= (r_x cos(\theta_x), r_x sin(\theta_x), x_{3,x}), \\ \mathbf{y} &= (r_y cos(\theta_y), r_y sin(\theta_y), y_{3,y}), \end{aligned} \tag{12}$$

where $\varphi(.) = \sqrt{r^*} sin(\theta^*/2)$, for each location, $(.)^*$, defined in polar coordinates.

The acoustic calculations have been performed with a porous FWH implementation with the porous surfaces located $1.5h$ away from upper and lower surfaces and $1.5h$ downstream of the trailing edge point as well implementing 12 using surface terms. The grid refinement in this area provides high quality resolution resulting in almost a third of all processors having control volumes cut by these porous surfaces. The point noise, figure 17, is computed using both approaches for the experimental boundary layer case. It is clear that the differences are slight. This points to the considerable attractiveness of our porous FWH methodology and the effectiveness of our dynamic endcap approach.

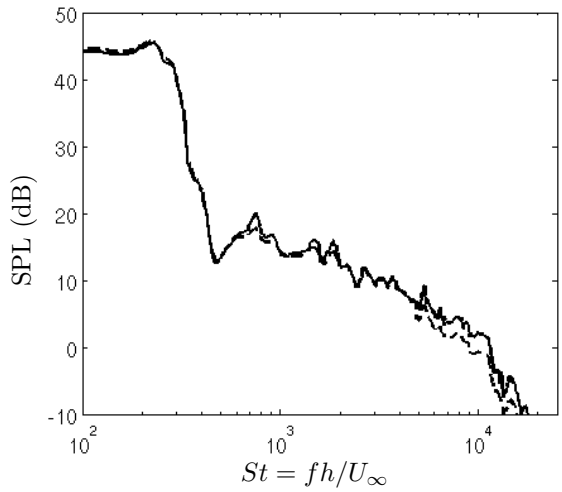

Figure 17: Point sound comparison using the half-plane Green's function with surface terms or the porous FWH approach.

CONCLUSION

We performed LES paired with our FWH method for a 45° beveled trailing edge. The flow fields show good agreement with experiment. The approach for obtaining this agreement involved using an oversized lower fidelity computation in order to obtain reasonable boundary conditions to achieve a comparable

coefficient of pressure with experiment. The use of the recycle rescale methodology was also important in order to get boundary layers that were in close agreement with the experiment. These boundary layers dictate both separation as well as fluctuating Reynolds stress components which were in close agreement with those previously observed.

Between the two boundary layer thicknesses, the vorticity shed into the wake is larger for the thinner boundary layer, but since it separates later, the values of $\vec{\omega} \times \vec{u}$ are lower. Also, this thinner boundary layer results in a smaller region of source distribution. On the lower surface of the trailing edge boundary layer separation happens at roughly the same location and $\partial^2 u'u'/\partial t^2$ is the dominant source term which is produced over a thinner region but is almost as intense and therefore produces comparable noise. This accounts for the increased noise in the upper half plane for the thicker boundary layer relative to the difference in the lower half plane between the the two thicknesses.

Our porous FWH methodology is shown to agree well with sound predicted using the surface terms and a half-plane Green's function. This points to the considerable promise of our methodology to predict the sound from turbulent flows and complex configurations.

ACKNOWLEDGMENTS

This work was supported by the United States Office of Naval Research (ONR) under Grant No. N00014-14-1-0304 with Dr. Ki-Han Kim as technical monitor. Computing resources were provided by the DoD HPCMP Open Research Systems, the Minnesota Supercomputing Institute, and in part by the National Science Foundation through XSEDE resources provided by the XSEDE Science Gateways program.

References

Blake, W.K. "A statistical description of pressure and velocity fields at the trailing edges of a flat strut". Technical report, DTIC Document, 1975.

Blake, W.K. "Mechanics of flow-induced sound and vibration". New York, page 9, 1986.

Blake, W.K. and Gershfeld, J.L. "The aeroacoustics of trailing edges". In Frontiers in Experimental Fluid Mechanics, pages 457–532. Springer, 1989.

Cox, J.S., Brentner, K.S., and Rumsey, C.L. "Computation of vortex shedding and radiated sound for a circular cylinder: subcritical to transcritical Reynolds numbers". Theoretical and Computational Fluid Dynamics, 12:233–253, 1998.

Crighton, D.G. "Radiation from a vortex filament motion near a half plane". Journal of Fluid Mechanics, 51(02):357–362, 1972.

Ffowcs-Williams, J.E. and Hawkings, D.L. "Sound generation by turbulence and surfaces in arbitrary motion". Philosophical Transactions of the Royal Society of London, 264A:321–342, 1969.

Gershfeld, J.L., Blake, W.K., and Knisely, C.W. "Trailing edge flows and aerodynamic sound". In AIAA Thermophysics, Plasmadynamics and Lasers Conference, San Antonio, Texas AIAA Paper, volume 3826, pages 2133–2140, 1988.

Howe, MS. "Contributions to the theory of aerodynamic sound, with application to excess jet noise and the theory of the flute". Journal of Fluid Mechanics, 71(4):625–673, 1975.

Lighthill, M.J. "On sound generated aerodynamically. part I: General theory". Proceedings of the Royal Society of London, A(211):564–587, 1952.

Lund, T.S., Wu, X., and Squires, K.D. "Generation of Turbulent Inflow Data for Spatially-Developing Boundary Layer Simulations". Journal of Computational Physics, 140(2):233–258, 1998.

Manoha, E., Troff, B., and Sagaut, P. "Trailing-Edge Noise Prediction Using Large-Eddy Simulation and Acoustic Analogy". AIAA Journal, 38(4):575–583, 2000. ISSN 0001-1452. doi: 10.2514/2.1015.

Marsden, A.L., Wang, M., Dennis, J.E., and Moin, P. "Trailing-edge noise reduction using derivative-free optimization and large-eddy simulation". Journal of Fluid Mechanics, 572:13, 2007.

Nitzkorski, Zane and Mahesh, Krishnan. "A dynamic end cap technique for sound computation using the ffowcs williams and hawkings equations". Physics of Fluids, 26(11):115101, 2014.

Oberai, A.A., Roknaldin, F., and J., Thomas. "Computation of Trailing-Edge Noise Due to Turbulent Flow over an Airfoil". AIAA Journal, 40(11):2206–2216, 2002.

Olson, S. and Mueller, T.J. "Phased array acoustic imaging of an airfoil trailing edge flow". In 11th International Symposium on Flow Visualization, 2004.

Revell, J.D., Prydz, R.A., and Hays, A.P. "Experimental study of airframe noise versus drag relationship for circular cylinders". Final report for NASA contract NAS1-14403, Lockheed Report 28074, 1977.

Shannon, D.W. and Morris, S.C. "Experimental investigation of a blunt trailing edge flow field with application to sound generation". Experiments in Fluids, 41(5):777–788, 2006.

Shannon, D.W., Morris, S.C., and Mueller, T.J. "Radiated sound and turbulent motions in a blunt trailing edge flow field". International Journal of Heat and Fluid Flow, 27(4):730–736, 2006.

Sinayoko, S., Wright, M.C.M., and Sandberg, R.D. "A generalized ffowcs-williams and hawkings formulation applied to flow simulations with vortical outflow.". In International Congress on Sound and Vibration, volume 22. Florence,Italy, 2015.

Singer, B.A., Brentner, K.S., and D.P .and Lilley-Lockard, G.M. "Simulation of Acoustic Scattering from a Trailing Edge". AIAA paper, 231:1999, 1999.

Verma, A. and Mahesh, K. "A Lagrangian Subgrid-scale Model with Dynamic Estimation of Lagrangian Time Scale for Large Eddy Simulation of Complex Flows". Physics of Fluids, 24(8):085101, 2012.

Wang, M. "Compuation of trailing-edge aeroacoustics with vortex shedding". Center for Turbulence Research: Annual Research Briefs, pages 379–388, 2005.

Wang, M. and Moin, P. "Computation of trailing-edge flow and noise using large-eddy simulation". AIAA Journal, 38(12):2201–2209, 2000.

Wang, M, Lele, S.K., and Moin, P. "Computation of quadrupole noise using acoustic analogy". AIAA Journal, 34(11):2247–2254, 1996.

Williams, J.E. and Hall, L.H. "Aerodynamic sound generation by turbulent flow in the vicinity of a scattering half plane". Journal of Fluid Mechanics, 40(04):657–670, 1970.

Yu, J.C. and Tam, W.C.K. "Experimental investigation of trailing edge noise mechanism". AIAA Journal, 16(10):1046–1052, 1978.